Original article

Fault-controlled oil and gas reservoir unit division based on graph

Cheng Zhou[1], Yifeng Fei[2], Xin He[2], Hanpeng Cai[2]*, Xingmiao Yao[2], Guangmin Hu[2]

[1]*School of Information and Communication Engineering, University of Electronic Science and Technology of China, Chengdu 611731, P. R. China*

[2]*School of Resources and Environment and Center for Information Geoscience, University of Electronic Science and Technology of China, Chengdu 611731, P. R. China*

Abstract:
Research on reservoir-unit division in fault-controlled oil and gas reservoirs is essential for analyzing reservoir hydrocarbon migration and accumulation. Currently, most research on reservoir-unit division has focused solely on the identification of faults and caves, employing three-dimensional spatial visualization or other methods for a simple analysis of their links. However, these approaches often lack a reasoning process that exploits the links between faults and caves for deeper insights. For such complex oil and gas reservoirs, a systematic analysis based on the interrelations between multiple geological factors is needed. Therefore, this paper proposes a graph-based method for reservoir-unit division in fault-controlled oil and gas reservoirs, enabling the representation of links between faults and caves, and it presents further systematic analysis to derive the reservoir-unit division results. A multi-attribute graph-clustering-based fault-extraction method is utilized to achieve comprehensive fault representations as fault entities. More reliable cave-instance segmentation results are obtained through attribute fusion, representing cavity entities. A graph incorporating fault and cave entities is then created. Fault entities are classified into several levels according to their spatial scale, and directed edges are utilized to represent connectivity links between faults and caves. Moreover, a connectivity analysis centered on caves was conducted using the created graph. Based on existing reservoir-unit knowledge and the cave-connectivity analysis results, reservoir-unit division was achieved. The proposed method provided reservoir-unit division results highly consistent with the information contained in seismic data, offering a new perspective for multielement integrated analysis in geophysical exploration.

1. Introduction

Fault-controlled oil and gas reservoirs (OGRs) are reservoirs whose formation and distribution are significantly influenced and controlled by faults. OGRs are widely distributed in regions including western China. Research on reservoir-unit (RU) division in fault-controlled OGRs aids in analyzing hydrocarbon migration and reservoir distribution, which primarily involves research on faults, karst caves (KCs), and their links.

Considerable research has been conducted on fault identification. Faults in seismic data are typically characterized by lateral discontinuities, and early studies primarily focused on finding such lateral discontinuities. Coherence is considered the most effective technique for fault identification. For instance, Bahorich and Farmer (1995) introduced the first-generation coherence attribute based on cross-correlation, which had high computational speed but poor noise resis-

tance. Furthermore, Marfurt et al. (1998) developed a second-generation coherence attribute based on multi-trace similarity, which effectively addressed the noise-resistance issue of the first generation while maintaining high computational speed and applicability. Moreover, Gersztenkorn and Marfurt (1999) proposed a third-generation coherence attribute based on an eigenstructure, providing more robust coherence estimates and generating higher-resolution results, but with higher computational complexity. Subsequently, more coherence-based methods were introduced, including local structure entropy-based coherence and fault likelihood (Cohen and Coifman, 2002; Hale, 2013). In addition to coherence, variance and curvature attributes have also been utilized for fault detection (Randen et al., 2001; Roberts, 2001). In recent years, with the rapid development of artificial intelligence (AI) and its impressive performance across various fields, researchers have increasingly focused on using deep-learning techniques for fault detection. Some researchers have approached fault detection as a classification problem. Di et al. (2018) proposed a two-dimensional (2D) fault-detection network based on a convolutional neural network (CNN). The input is a 2D seismic data patch; the output, a classification result for the central point of the patch. This method demonstrated better performance than support vector machine and multilayer perceptron. Guitton (2018) proposed a three-dimensional (3D) fault-detection network based on CNN, where the input is a 3D seismic data block, and the output is the classification result for the block's central point. In addition, Xiong et al. (2018) proposed a CNN-based fault-detection network that uses three 2D seismic data patches centered on the target point (inline, crossline, and time slices) as input and outputs the probability that the target point belongs to a fault. This network was trained using automatic fault-picking results as fault labels and demonstrated better fault continuity than coherence attributes. Others have approached the problem as semantic segmentation, achieving end-to-end fault identification. For example, Wu et al. (2019) developed a 3D fault-detection network based on UNet to detect faults from 3D seismic data. The network was trained on synthetic 3D seismic data and achieved superior results to some traditional methods in multiple field data. Furthermore, Liu et al. (2020b) trained a residual UNet on synthetic data for 3D fault detection, demonstrating more accurate fault identification than coherence-based and UNet methods. Zhou et al. (2021) proposed a progressive learning framework to update the training dataset, reducing discrepancies between the training and prediction data. They also introduced a fault-label correctness metric to improve the framework's stability. Over time, research on fault identification based on AI has gradually become mainstream, outperforming traditional methods including seismic attribute-based approaches on some datasets. Moreover, semantic segmentation-based methods are becoming a key focus, with increasing attention being paid to their performance on more complex field data. Most existing fault identification networks often require data to be partitioned into blocks to meet the input-size requirements of the network. This way, the data information that networks can utilize for fault identification comes from at most one data block, which may limit the networks' performance in complex situations.

Introducing more comprehensive data information can help improve the fault identification performance in some complex fault situations.

Fault extraction can yield the distribution of each fault from fault-detection results. One method is to pinpoint fault lines on 2D slices or sections and then group them together to form 3D faults. Zhang et al. (2014) proposed a semi-automatic fault-interpretation workflow, where coherence or other discontinuity attributes are skeletonized to extract fault lines on time slices. These lines are then grouped and utilized to create 3D fault surfaces via triangulation. Moreover, Zhang and Lou (2020) introduced a method to automatically create faults by analyzing the topological links of seismic fault attributes on inline, crossline, and time slices. Applications on public datasets demonstrated the accuracy of this method in generating fault surfaces. In addition, Lou et al. (2021) grouped 2D fault lines based on connectivity and exclusivity and merged the lines across time slices through topological analysis to form fault surfaces. Experiments showed that this method effectively handled conjugate faults in seismic data. Another method directly processes faults in 3D space. Hale (2013) utilized a method similar to Crease Surfaces to extract ridge surfaces from the fault-likelihood attribute, representing fault surfaces with quadrilateral meshes (Schultz et al., 2009). However, this method has limitations when dealing with intersecting faults, often resulting in holes at intersections. Wu and Hale (2016) further improved on this method using a simple linked data structure to create faults and interpolating missing areas, successfully creating complete fault surfaces that can deal with crossing faults. Zhou et al. (2022, 2024b) proposed using fault graphs to obtain the complete distribution of faults, effectively addressing complex fault situations. Clearly, two critical study areas exist in fault extraction: the integrity of extracted faults and the ability to handle complex faults. The aforementioned studies have improved performance in these two aspects to varying degrees. Among these approaches, using fault graphs for fault extraction represents a promising direction. By representing fault distributions as fault graphs, we can effectively utilize the interrelationships between multiple faults to analyze complete faults from a broader perspective. This method holds great potential in addressing complex fault situations.

Research on cave detection is similar to that on fault detection. Researchers primarily use seismic attributes to characterize KCs-including coherence, structural curvature, and spectral decomposition-to highlight karst features in 3D seismic data (Bahorich and Farmer, 1995; Roberts, 2001; Chen, 2016). For instance, Li (2012) identified the typical reflection characteristics of cavities at different depths and utilized a combination of high-resolution coherence attributes and impedance inversion bodies to predict the distribution of cavities between wells. Moreover, Halpert et al. (2009, 2014) proposed a method that prioritizes attribute fusion and segmentation to detect cavities, based on the observation that different attributes of cavities emphasize distinct aspects of their features. Chen et al. (2015) improved the ability to detect weakly reflective cavities in seismic data by employing diffraction wave-separation imaging techniques. In addition,

Li et al. (2016) created physical models of cavities with multiple scales and filling patterns and conducted forward modeling to refine the influencing factors of cavity seismic responses, reducing the ambiguity in cavity detection. Recently, researchers have explored AI-based methods for cave detection. For instance, Wu et al. (2020) introduced a 3D intelligent detection network for finding and analyzing paleokarst collapse features, improving detection accuracy and efficiency. Moreover, Zhang et al. (2022) incorporated Bayesian deep learning into the seismic characterization of deeply buried paleocaves, enhancing the model's capability to pinpoint complex geological bodies through uncertainty quantification, integration of geological priors, and probabilistic data-driven analysis while also improving transparency and reliability. Zhu et al. (2024) utilized simulated the seismic responses of various paleokarst structures to generate high-quality training data for intelligent detection networks, achieving robust identification and generalization of features in field seismic data. Subsequently, Gui et al. (2024) enhanced the model's ability to capture fault and karst features through attribute fusion, improving resistance to noise and making the detection results more reliable. Most of the aforementioned methods are tailored to specific study areas for targeted KC identification. Therefore, in practical applications, we must select appropriate methods based on the characteristics of the KCs in the study area. Alternatively, an attribute fusion method can be adopted, selecting multiple attributes that best highlight the KCs in the study area. Another option is to create synthetic data with features similar to those of KCs in the study area to train intelligent KC identification networks.

Research on fault-controlled OGRs has mostly focused on the identification of faults and KCs, using 3D visualization or other methods to perform simple analyses of the links between them. To address the complexity of ultra-deep fracture-controlled karst reservoirs, Liu et al. (2020a) proposed a multilevel characterization method-including cavity carving, identification of dissolved cavities, and delineation of fracture zones-significantly improving reservoir-detection accuracy. Furthermore, Hu et al. (2023) utilized seismic wave impedance inversion and frequency-domain detection of multi-scale faults to precisely characterize the spatial distribution of cavities, dissolved cavities, and multi-scale faults, and they further conducted 3D geological modeling of these features. Similarly, Gui et al. (2024) achieved reservoir-detection results by directly integrating accurately identified faults and cavities. However, further reasoning based on these links in these methods is lacking. The challenge lies in effectively representing the links between faults and KCs and enabling relevant reasoning, calculations, and analysis.

To address this, this paper proposes a graph-based method for RU division, achieving a representation of the links between faults and KCs based on accurate identification and then presenting a systematic analysis conducted to obtain RU division results. Using AI-based fault identification, our method applies a multi-attribute graph-clustering method to extract complete fault characterizations from the fault identification results, serving as fault entities. Then, attribute fusion is utilized to obtain more reliable KC instance segmentation
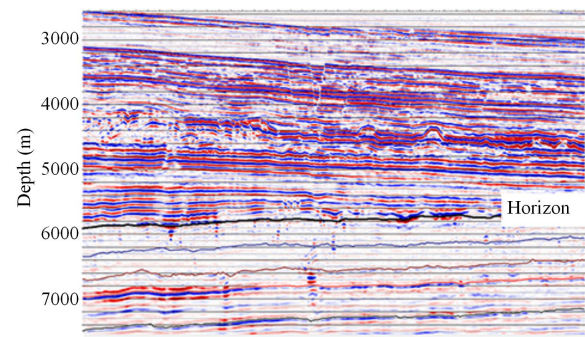

Fig. 1. Illustration of an inline section from a work area in western China.

results, which serve as the KC entities. A graph containing fault and KC entities is then created, with faults classified into different levels by spatial scale and directed edges representing the connectivity between faults and KCs, thus linking faults and KCs. Furthermore, the created graph facilitates a connectivity analysis of KCs. Based on existing knowledge of RUs and the connectivity analysis results for KCs, the final RU division was obtained. The proposed method provided RU division results aligning well with the information contained in seismic data, indicating that it offers a new method to multielement integrated analysis in geophysical exploration.

2. Data description

The study data were from western China, with an inline section shown in Fig. 1. The region above the horizon marked by the black line consists of sandstone and mudstone deposits, while the region below is carbonate rock. Our target area was the carbonate region below the horizon marked by the black line, where fault-controlled reservoirs had developed. As seen in Fig. 1, there were numerous "beaded" reflection zones below the marked horizon, which indicate KCs. Specifically, in the study data, the number of inlines was 421, the number of crosslines was 761, and each trace contained 100 sampling points, corresponding to a depth range of 5,600–7,600m, with a sampling interval of 5m in the depth dimension.

3. Methodology

In this section, the proposed method is described in detail. The workflow of our method consists of two main parts: graph creation and RU division. Graph creation involves finding fault and KC entities from seismic data and representing the links between them. The RU division is then performed by inferring the division results in the created graph.

The graph to be created contains two types of entities: faults and KCs. Faults play a vital role in controlling the migration, accumulation, or destruction of oil and gas, while KCs are important underground reservoirs for oil and gas. Therefore, this section provides a detailed description of the graph-creation process, including the identification of fault entities, the identification of KC entities, and the determination of the edge links between these entities.

Therefore, this section introduces the proposed method in four steps: identification of fault entities, identification of KC
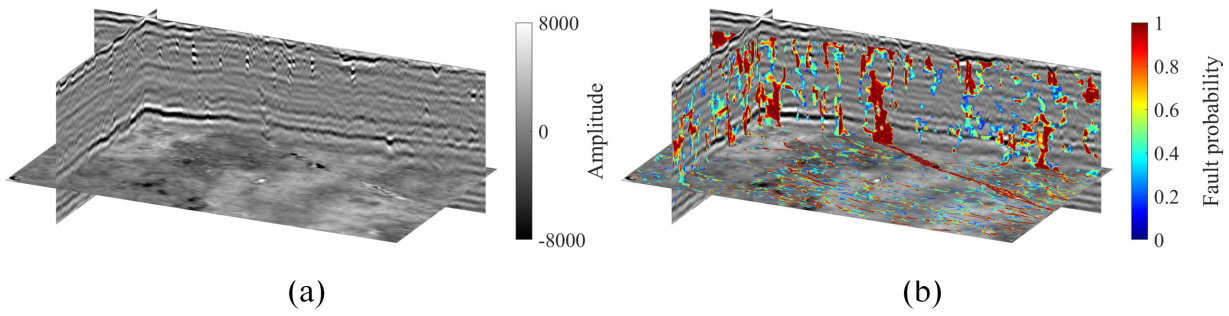
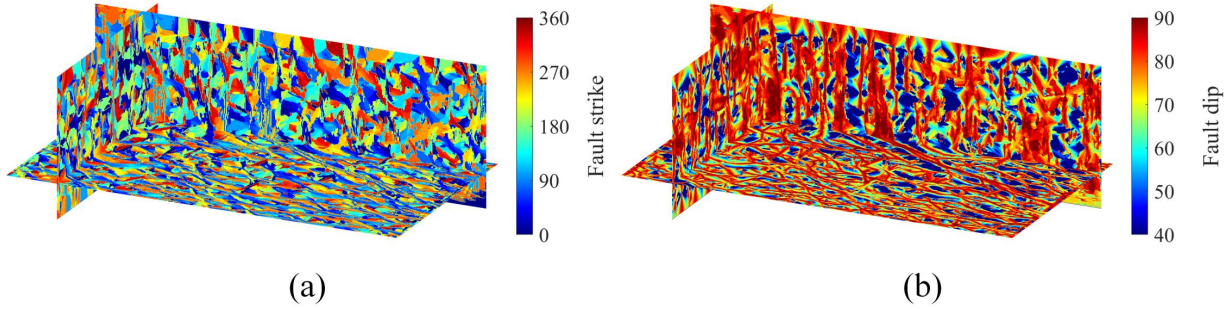**Fig. 2.** (a) The seismic data and (b) the computed fault attribute.

Fig. 3. (a) The fault strike data and (b) the fault dip data.

entities, graph creation, and RU division.

3.1 Identification of fault entities

Fault imaging is the foundation for obtaining fault entities. Since AI-based methods have shown remarkable performance in existing fault identification research, achieving better results on some field data compared with traditional fault identification methods, faults in the study area are detected with an intelligence-based method. When using a fault intelligent detection network to process field data, it is often necessary to divide the data into blocks to meet the network's input-size requirements. Fault detection is then performed on each data block, and the results are recombined to produce fault-detection results for the entire data. Hence, the network can utilize, at most, the information in a single data block for fault detection, which severely limits its effectiveness in handling complex fault situations. More complex fault situations require the incorporation of additional data information. Zhou et al. (2024a) introduced a feature fusion module into the fault-detection network, which incorporates information from surrounding data blocks into the fault-detection process for the target data block. This expands the range of available data information, significantly enhancing the continuity and noise resistance of fault detection under complex fault situations. Given the complexity of faults in the study area, this method was applied to the seismic data shown in Fig. 2(a), and the corresponding fault-detection result is shown in Fig. 2(b). Although some noise was present in some areas, overall, relatively good fault continuity was observed.

The fault attribute provides the probability value for each data point belonging to a fault, and it is necessary to extract

each fault from the data and take each fault as a fault entity in the created graph. In this paper, the distribution of faults was represented using fault point sets. Therefore, the first step was to extract fault points from the fault attribute. A scanning method was applied to estimate the fault orientations from the fault-attribute data, including the fault strike and dip (Hale, 2013; Wu and Zhu, 2017). The calculation formula for this process is as follows:

$$(\varphi, \theta) = \underset{(\varphi,\theta)\in\varphi_{set}\times\theta_{set}}{\arg\min} f * g_{\varphi,\theta} \tag{1}$$

where $\times$ denotes the Cartesian product, and $*$ denotes the convolution operation. φ_{set} and θ_{set} are two predefined sequences of angles for the strike and dip that had to be processed by scanning, respectively. f represents the obtained fault-detection result, and $g_{\varphi,\theta}$ denotes a 3D spatial filter, whose spatial shape is defined by φ and θ. The computed fault strike and dip are shown in Figs. 3(a) and 3(b), respectively. The fault-attribute data were skeletonized to retain the fault points located at the ridges. Since the fault attribute was a fault-probability volume predicted by a neural network, a threshold of 0.5 was utilized to further filter the skeletonized result, and the results are shown in Fig. 4. It can be seen in Fig. 4 that the filtered skeletonized result aligns well with the fault locations in the seismic data. The retained data points in the filtered skeletonized result represent the fault points.

Furthermore, the obtained fault points were grouped based on the similarity of their orientations. Since the faults in the study area are relatively complex, stricter constraints were applied during the fault-points grouping process. Specifically, fault points grouped had to have very similar fault orientations
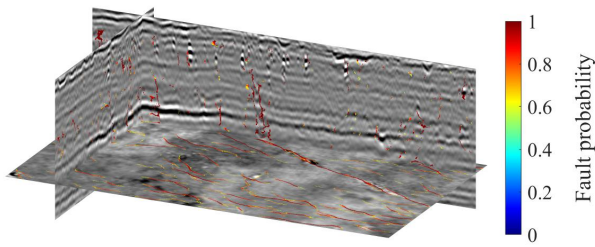
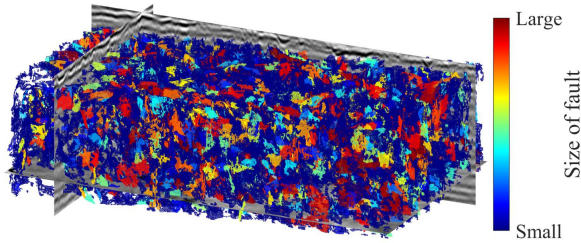**Fig. 4**. The filtered skeletonized fault attribute.

Fig. 5. The fault-point groups in 3D space.

Fig. 6. The created fault graph.

Each fault node in the newly obtained fault graph was treated as a fault entity, which represents a relatively complete fault.

3.2 Identification of KC entities

In the study area, compared with faults, KCs exhibit more distinct characteristics in seismic data, presenting typical "beaded" features. Therefore, an attribute fusion method was applied to pinpoint KCs from seismic data. The root-mean-square (RMS) amplitude attribute and gradient-structure tensor (GST) attribute were calculated separately. As shown in Fig. 9, both attributes provided good imaging of the KCs. The RMS attribute highlighted regions with strong amplitude responses, which may indicate the presence of karst features including caves. However, it showed limitations in resolving the finer details of complex karst structures and was susceptible to noise, potentially leading to misinterpretations if not properly filtered. The GST attribute, contrastingly, captured subtle variations in seismic data, making it particularly effective for finding structurally complex KCs. It provided clearer boundary delineations, aiding in the interpretation of the extent and shape of caves. In addition, it integrates filtering and statistical methods that help mitigate noise. Nevertheless, under high noise levels, the GST attribute could still be affected, potentially resulting in mis-identifications where noise or non-geological features were mistaken for KCs.

Given that the study area is deep underground, resulting in low-quality seismic data, the fusion of the two attributes was performed to achieve a more reliable outcome. Both RMS and GST attributes were binarized. After multiple experiments, the thresholds 2,000 and 0.00045 were selected for the binarization of the two attributes. The intersection of the two binarized results was taken to achieve an attribute fusion analysis for KC identification. Different KCs were distinguished based on connectivity, with the results shown in Fig. 10. Fig. 11 displays the identification result of KCs on three crossline sections, which generally align with the seismic data. Each KC in Fig. 10 could be treated as a KC entity.

3.3 Graph creation

Based on the geological process of KC formation, it can be inferred that large faults connect to smaller faults, which,

to ensure that all fault points in each group belonged to the same fault, preventing the introduction of erroneous information into subsequent analyses. The obtained fault-point groups are shown in Fig. 5.

Each fault-point group represents only a part of a fault, not a complete fault. The groups located on the same fault had to be merged so that the merged groups would represent the complete faults. The merging process was as follows: Each fault-point group was treated as a node to create a fault graph, and edges were connected between fault nodes based on spatial distance constraints (with a selected distance constraint of 10 in our experiment). The attributes of the edges represent the links between the fault segments indicated by the fault nodes. The edge links were categorized into three types: same (two nodes in one fault), non-same (two nodes not in one fault), and other. Two fault nodes connected by the "same" edge had to form a continuous and smooth surface in 3D space. For fault nodes connected by a "non-same" edge, their spatial distributions had to meet one of the following: there must be a significant difference in fault orientation between their adjacent areas, or there must be an overlap between them in the direction perpendicular to the fault. Based on these criteria, the attributes of the created edges could be evaluated. In this way, a multi-attribute fault graph was obtained, as shown in Fig. 6. Our goal was to group nodes connected by "same" edges together as much as possible under the strict constraint that nodes connected by "non-same" edges would not be grouped. To achieve this, we applied a multi-attribute graph-clustering method proposed in Zhou et al. (2024b) to solve this problem, resulting in a new fault graph. The merging process is shown in Fig. 7(a), and the fault graph is shown in Fig. 7(b). The 3D distribution of fault points corresponding to each node in the newly obtained fault graph is shown in Fig. 8. By comparing Figs. 5 and 8, we can see that the faults become more complete.
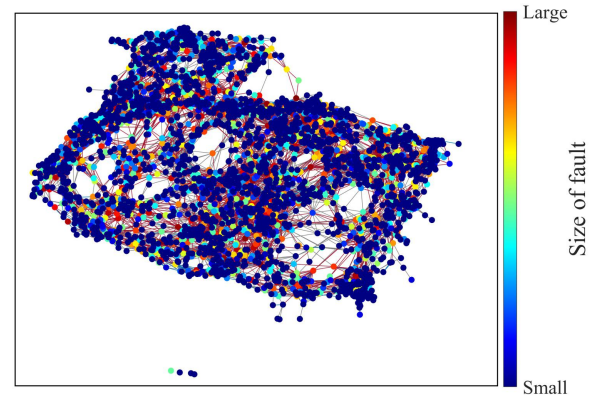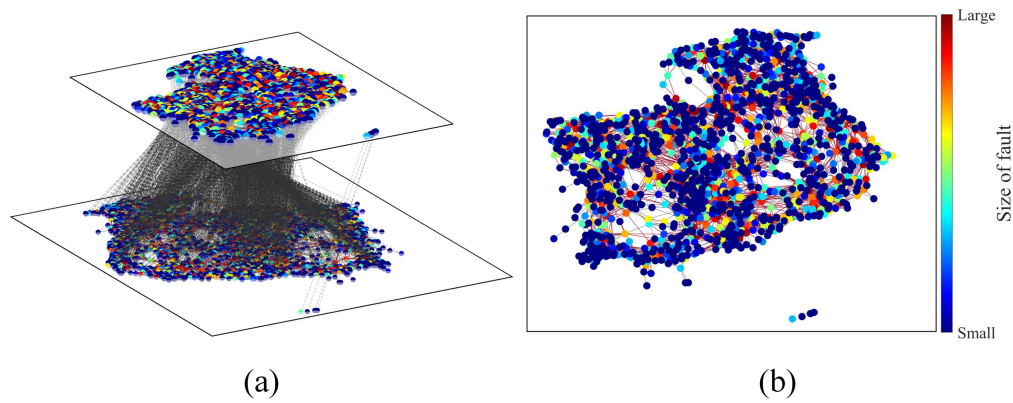
(a)   (b)

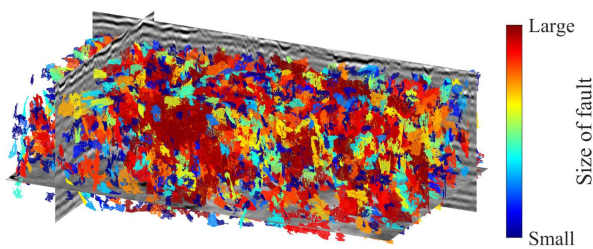**Fig. 7**. (a) The merging process and (b) the newly obtained fault graph.

Fig. 8. The fault-point groups in 3D space corresponding to the new fault graph.

Table 1. Fault-level classification criteria and the number of faults in each level.

Level	Range of fault-point number	Fault number
1	$> 10,000$	13
2	$(5,000, 10,000]$	39
3	$(1,000, 5,000]$	450
4	$(500, 1,000]$	448
5	< 500	853

in turn, link to KCs. Therefore, faults need to be classified into different levels according to their spatial scale to facilitate subsequent analysis of the connectivity between faults and KCs.

The fault-point number in each fault entity reflects the spatial scale of the fault. A statistical analysis was conducted on the distribution of fault-point counts across all fault entities. Based on this analysis, faults were classified into five levels according to the fault-point number: level 1, level 2, level 3, level 4, and level 5, corresponding to fault-point counts of over 10,000, 5,000-10,000, 1,000-5,000, 500-1,000, and below 500, respectively. The fault-level classification criteria for each fault level and the corresponding number of faults are shown in Table 1. The 3D spatial distributions of fault points for each fault level are shown in Fig. 12. From Figs. 12(a)-12(e), it is evident that from level 1 to level 5, the spatial scale of the faults decreased progressively. For levels 4 and 5, the

spatial distribution of faults more closely resembled small-scale fractures.

Based on the fault-level classification, the graph could be created as follows: the identified fault entities and KC entities were utilized as nodes, and edges were created between nodes that were spatially close to each other. The edges were directed, with their direction defined as pointing from lower-level faults to higher-level faults (level 1 for the highest level) or from KCs to other nodes. The direction of the edges aligned with the conclusions drawn from the geological processes of the KC formation mentioned earlier: large faults connected to smaller faults, which, in turn, linked to KCs. This method represents the geological process of KC formation as a directed graph composed of faults and KCs, facilitating a subsequent connectivity analysis centered on KCs. The created fault-KC directed graph is shown in Fig. 13.

3.4 RU division

Based on the created graph, a connectivity analysis centered on KCs could be conveniently performed. Since the graph was directed, it was convenient to determine which nodes a specific KC node was connected to via directed edges. According to the graph-creation process described earlier, the connected nodes of a KC strictly follow the pattern of larger faults connecting to smaller faults, which then connect to the KC. The connectivity-analysis results of two KC nodes are shown in Fig. 14, where the left two figures display the connected nodes in the created graph, and the right two figures show the corresponding spatial distribution of fault nodes and KC nodes in 3D space.

RU division could then be performed based on the connectivity-analysis results of KCs. Building on the earlier conclusion inferred from the geological process of KC formation, further reasoning could be done: The KCs in the same RU had to connect to the same fault of a certain scale (medium-sized fault). In such cases, these KCs were interconnected through small or medium faults, resulting in good connectivity. This would enable more direct and significant interactions between the caves, facilitating the formation of a stable RU for hydrocarbon accumulation. During oil and gas development, it may be sufficient to drill a well into one of the KCs to exploit
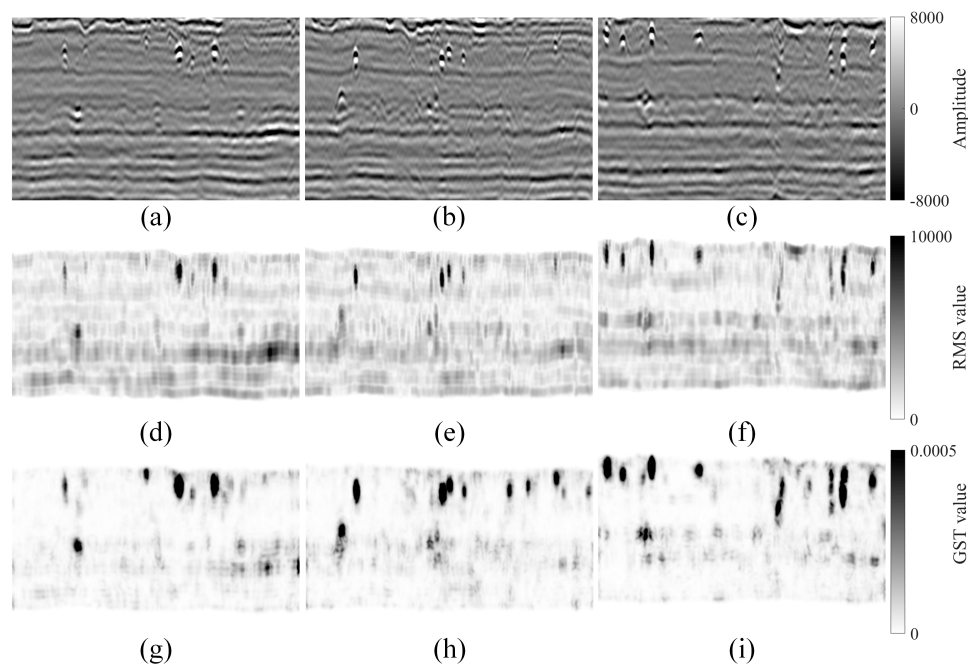
Fig. 9. The seismic data, the RMS attribute, and the GST attribute and seismic data in three crossline sections: (a)-(c) the seismic data, (d)-(f) the RMS attribute, and (g)-(i) the GST attribute. The first column to the third column correspond to crossline 221, crossline 259, and crossline 566, respectively.
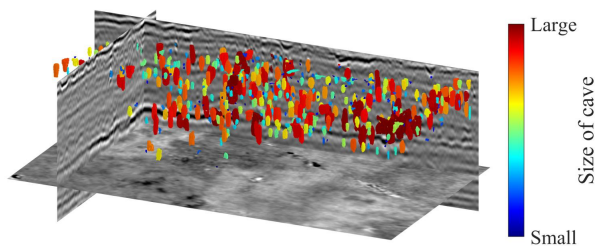

Fig. 10. The identified KCs in 3D space.

the hydrocarbon resources contained in all connected caves. Given the current limitation of seismic data, a simplified method was adopted to classify faults of levels 2 and 3 as medium-sized faults based on their spatial scale. Thus, in the KC connectivity-analysis results, KCs that were simultaneously connected to a level-2 or level-3 fault were grouped. Using this method, all KCs could be grouped, with each group representing a RU. The distribution of KCs in four RUs on a horizon slice is shown in Fig. 15. It can be observed that the KCs in each RU were spatially close to each other, aligning well with our understanding of such geological structures.

4. Results and discussion

The distributions of KCs in the four RUs on a horizon slice are shown in Fig. 15. As previously mentioned, KCs in the same RU are spatially clustered, which aligns with the actual geological conditions. To analyze the specific role of faults in RU division, the background in Fig. 15 replaced seismic data on the horizon slice with fault attributes on the horizon slice. The updated results are shown in Fig. 16. From Figs. 16(a)-

16(d), it can be observed that the distribution of KCs in the same RU generally corresponded to the spatial distribution of a specific fault. This supports the earlier inference that KCs in the same RU are simultaneously connected to a medium-sized fault, confirming that the RU division aligned with the expected results. To further explore the link between KCs and faults in the same RU, we visualized the RUs (KCs) and their connected faults in the created graph and their corresponding distribution in 3D space, as shown in Fig. 17, where the left four figures display the connectivity links in the created graph, while the right four figures show the corresponding 3D spatial distributions. From the right four figures in Fig. 17, it is clear that the KCs in a RU were spatially clustered and that their spatial distribution closely aligned with the spatial distribution of surrounding faults. The number of KCs within the four RUs shown in Fig. 17 and the number of faults of each level connected to these KCs are presented in Table 2. It can be observed that the number of medium-sized faults (levels 2 and 3) in each RU is relatively higher. The connected medium-sized faults essentially define the spatial distribution range of each RU. It can also be observed in Fig. 17 that the connected faults generally extended to deeper regions, which is consistent with the understanding of oil source faults. The hydrocarbons came from the deeper layers of the earth, and through the faults that extend to the deeper layers, the hydrocarbons could be transported to and stored in the caves located in shallower locations. Therefore, from the distribution of faults surrounding the RU, it is highly likely that the KCs in the identified RUs are filled with hydrocarbons.

The current study was based on seismic data, determining connectivity through the spatial link between faults and KCs.
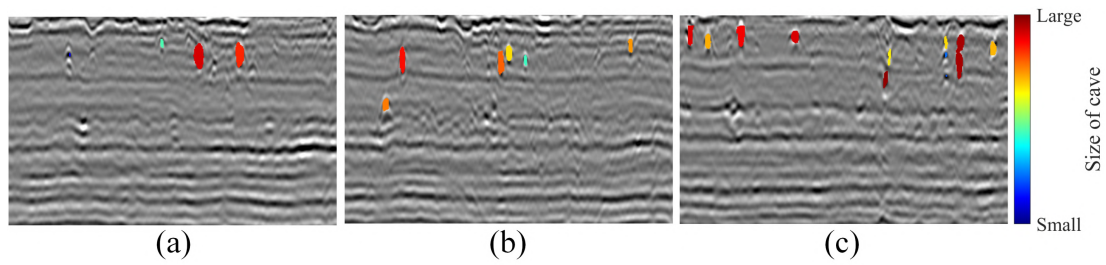
Fig. 11. The identified KCs in (a) crossline 221, (b) crossline 259 and (c) crossline 566.
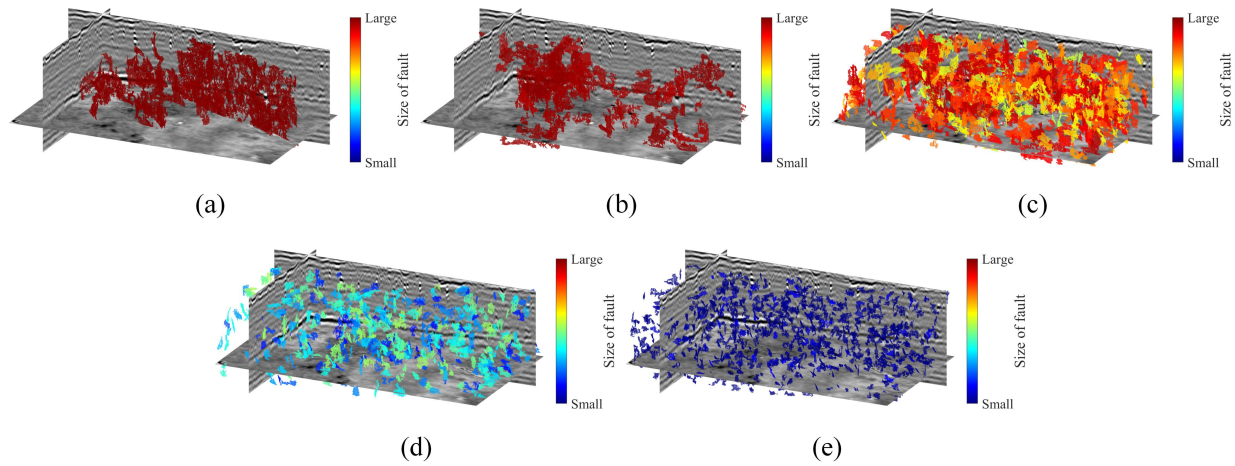

Fig. 12. Fault points contained in five fault levels in 3D space: (a) level 1, (b) level 2, (c) level 3, (d) level 4 and (e) level 5.
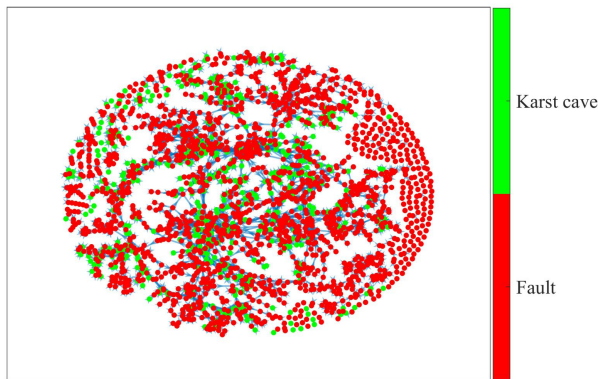

Fig. 13. The created fault-KC directed graph.

Table 2. The number of caves and faults in the four RUs in Fig. 17.

Cave	Fault number					
	Level 1	Level 2	Level 3	Level 4	Level 5	Sum
6	3	7	22	3	5	40
11	28	6	14	5	5	58
11	7	8	33	8	9	65
12	31	16	14	4	4	69

However, in practical situations, the internal connectivity of faults and KCs is influenced by other factors, including infill materials and porosity. Therefore, in the existing framework, production data can be integrated. For example, information on infill materials and porosity can be utilized to assess oil and gas migration in faults and KCs. The assessment results can then be incorporated as attributes of fault and KC entities in the created graph, further refining the connectivity analysis results.

5. Conclusion

A graph-based fault-controlled RU division method was proposed for OGRs, which identifies faults and KCs separately from seismic data and uses a graph to integrate the results, obtaining RU division results. For fault identification, a multi-attribute graph-clustering-based fault-extraction method is employed to achieve complete fault characterization from fault imaging results. In KC identification, attribute fusion is utilized to obtain more reliable cave-instance segmentation results. The fault and KC results are then combined by creating a graph that links them, with faults classified into different levels by spatial scale and directed edges representing the connectivity between faults and KCs. This method enables connectivity analysis of KCs. Based on existing knowledge of RUs and the connectivity analysis results, RU divisions were achieved. Thus, the proposed method offers a new perspective for multi-element integrated analysis in geophysical exploration.

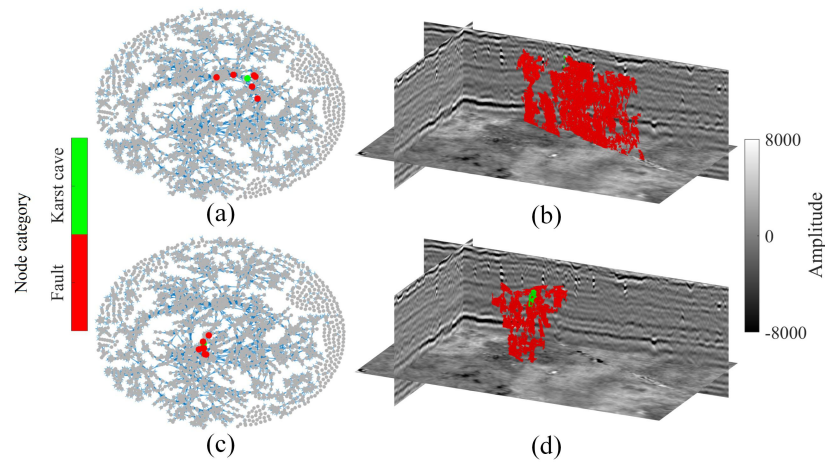Note that, as the current study was based on seismic data,

Fig. 14. The connectivity-analysis results of two KC nodes: (a) the connected node of one KC node in the graph and (b) the corresponding 3D spatial distribution of these nodes, and (c) the connected node of another KC node in the graph and (d) the corresponding 3D spatial distribution of these nodes.
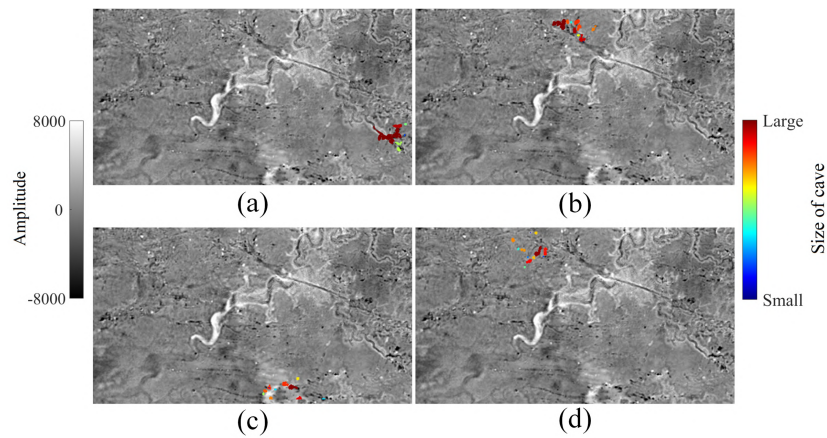

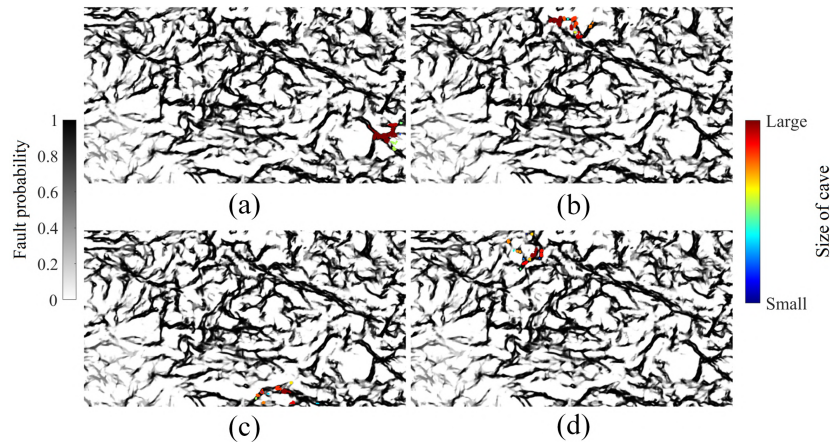**Fig. 15**. Four RUs on a horizon slice: (a), (b), (c) and (d) each correspond to a RU.

Fig. 16. Four RUs on a horizon slice with the background of the fault identification results: (a)-(d) each correspond to a RU.
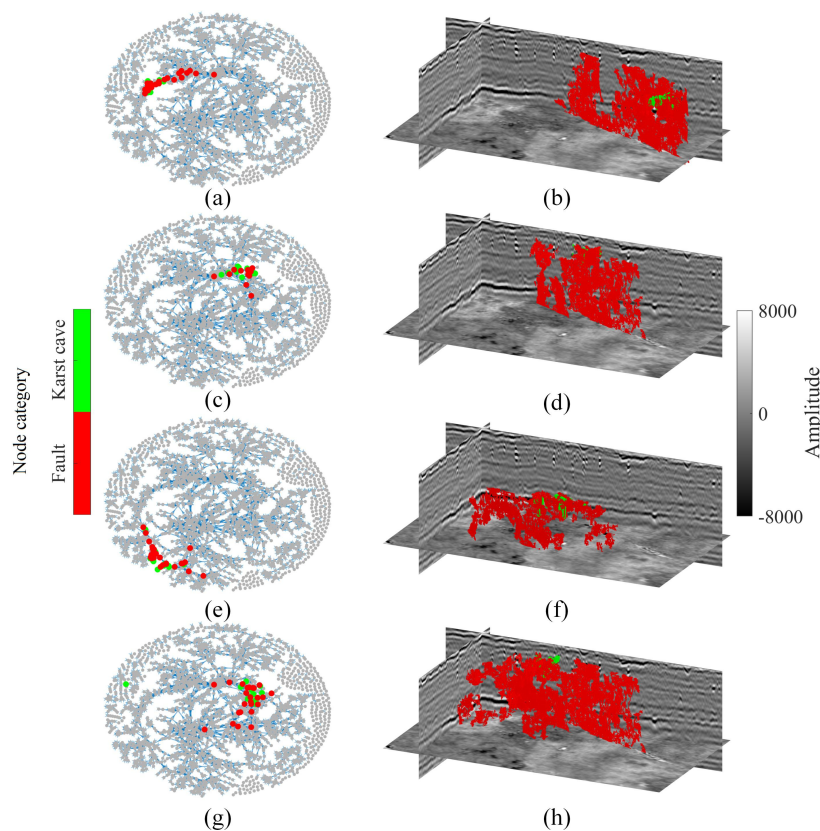
Fig. 17. Four RUs (KCs) and their connected faults: (a), (c), (e), and (g) are faults and KCs in the created graph, and (b), (d), (f) and (h) are the corresponding distributions in 3D space.

the validity of the results requires further verification. In future studies, production data can be incorporated to add more information to the created graph, yielding analysis results that better align with actual production conditions.

Acknowledgements

Conflict of interest

The authors declare no competing interest.

References

Bahorich, M., Farmer, S. 3-D seismic discontinuity for faults and stratigraphic features: The coherence cube. The Leading Edge, 1995, 14(10): 1053-1058.

Chen, M., Deng, G., Zhu, S., et al. Application of diffraction wave separation and imaging technique in weak seismic reflection of carbonate reservoir prediction in tahe oilfield. Geophysical Prospecting for Petroleum, 2015, 54(2): 234-240. (in Chinese)

Chen, Y. Probing the subsurface karst features using time-frequency decomposition. Interpretation, 2016, 4(4): T533-T542.

Cohen, I., Coifman, R. R. Local discontinuity measures for 3-D seismic data. Geophysics, 2002, 67(6): 1933-1945.

Di, H., Wang, Z., AlRegib, G. Seismic fault detection from post-stack am plitude by convolutional neural networks. Paper Presented at EAGE Conference and Exhibition, Copenhagen, Denmark, 11-14 June, 2018.

Gersztenkorn, A., Marfurt, K. J. Eigenstructure-based coherence computations as an aid to 3-D structural and stratigraphic mapping. Geophysics, 1999, 64(5): 1468-1479.

Guitton, A. 3D convolutional neural networks for fault interpretation. Paper Presented at EAGE Conference and Exhibition, Copenhagen, Denmark, 11-14 June, 2018.

Gui, Z., Zhang, J., Zhang, Y., et al. Characterization of fault-karst reservoirs based on deep learning and attribute fusion. Acta Geophysica, 2024, in Press https://doi.org/10.1007/s11600-024-01420-5.

Hale, D. Methods to compute fault images, extract fault surfaces, and estimate fault throws from 3D seismic images. Geophysics, 2013, 78(2): O33-O43.

Halpert, A. D., Clapp, R. G., Biondi, B. Seismic image segmentation with multiple attributes. Paper Presented at SEG Annual meeting, Houston, USA, 25-30 October, 2009.

Halpert, A. D., Clapp, R. G., Biondi, B. Salt delineation

via interpreter-guided 3D seismic image segmentation. Interpretation, 2014, 2(2): T79-T88.

Hu, X., Zheng, W., Zhao, X., et al. Quantitative characterization of deep fault-karst carbonate reservoirs: A case study of the yuejin block in the tahe oilfield. Energy Geoscience, 2023, 4(3): 100153.

Liu, B., Qi, L., Li, Z., et al. Spatial characterization and quantitative description technology for ultra-deep fault-karst reservoirs in the shunbei area. Acta Petrolei Sinica, 2020a, 41(4): 412. (in Chinese)

Li, F., Wei, J., Di, B., et al. Seismic physical model of carbonate cavern reservoirs. Oil Geophysical Prospecting, 2016: 272-280. (in Chinese)

Liu, N., He, T., Tian, Y., et al. Common-azimuth seismic data fault analysis using residual unet. Interpretation, 2020b, 8(3): SM25-SM37.

Li, Y. Ordovician carbonate fracture-cavity reservoirs identification and quantitative characterization in tahe oilfield. Journal of China University of Petroleum (Edition of Natural Science), 2012, 36(1): 1-7. (in Chinese)

Lou, Y., Zhang, B., Yong, P., et al. Semiautomatic fault-surface generation and interpretation using topological metrics. Geophysics, 2021, 86(3): O13-O27.

Marfurt, K. J., Kirlin, R. L., Farmer, S. L., et al. 3-D seismic attributes using a semblance-based coherency algorithm. Geophysics, 1998, 63(4): 1150-1165.

Randen, T., Pedersen, S. I., Sønneland, L. Automatic extraction of fault surfaces from three-dimensional seismic data. Paper Presented at SEG Annual meeting, San Antonio, USA, 9-14 September, 2001.

Roberts, A. Curvature attributes and their application to 3D interpreted horizons. First Break, 2001, 19(2): 85-100.

Schultz, T., Theisel, H., Seidel, H. P. Crease surfaces: From theory to extraction and application to diffusion tensor MRI. IEEE Transactions on Visualization and Computer Graphics, 2009, 16(1): 109-119.

Wu, X., Hale, D. 3D seismic image processing for faults. Geophysics, 2016, 81(2): IM1-IM11.

Wu, X., Liang, L., Shi, Y., et al. Faultseg3D: Using synthetic data sets to train an end-to-end convolutional neural network for 3D seismic fault segmentation. Geophysics, 2019, 84(3): IM35-IM45.

Wu, X., Yan, S., Qi, J., et al. Deep learning for characterizing paleokarst collapse features in 3-D seismic images. Journal of Geophysical Research: Solid Earth, 2020, 125(9): e2020JB019685.

Wu, X., Zhu, Z. Methods to enhance seismic faults and construct fault surfaces. Computers & Geosciences, 2017, 107: 37-48.

Xiong, W., Ji, X., Ma, Y., et al. Seismic fault detection with convolutional neural network. Geophysics, 2018, 83(5): O97-O103.

Zhang, B., Liu, Y., Pelissier, M., et al. Semiautomated fault interpretation based on seismic attributes. Interpretation, 2014, 2(1): SA11-SA19.

Zhang, B., Lou, Y. Automatic seismic fault surfaces construction using seismic discontinuity attribute. Paper Presented at SEG Annual meeting, online, 11-16 October, 2020.

Zhang, G., Lin, C., Ren, L., et al. Seismic characterization of deeply buried paleocaves based on bayesian deep learning. Journal of Natural Gas Science and Engineering, 2022, 97: 104340.

Zhou, C., Fei, Y., Li, D., et al. Fault detection from a large perspective with transformers. IEEE Transactions on Geoscience and Remote Sensing, 2024a, 62: 1-15.

Zhou, C., Zhou, R., Cai, H., et al. Fault surface extraction based on multi-relationship graph clustering. IEEE Transactions on Geoscience and Remote Sensing, 2024b, 62: 1-25.

Zhou, C., Zhou, R., Zhan, X., et al. Fault surface extraction from a global perspective. Geophysics, 2022, 87(5): IM189-IM206.

Zhou, R., Yao, X., Hu, G., et al. Learning from unlabelled real seismic data: Fault detection based on transfer learning. Geophysical Prospecting, 2021, 69(6): 1218-1234.

Zhu, D., Guo, R., Li, X., et al. Paleokarst caves recognition from seismic response simulation to convolutional neural network detection. Geophysics, 2024, 89(1): WA265-WA277.